SUPPLEMENTAL INFORMATION

Eddy-edge submesoscale dynamics drive chlorophyll exchange across the mixed-layer base

Changjie Wang, Fenfen Liu

*** Corresponding author: E-mail address: lfenfen@mail.sysu.edu.cn (F. Liu).**

Mesoscale modulation of mixed layer depth and instability diagnostics near the mixed-layer base

The main text identifies eddy-edge frontal environments as preferred locations for strong vertical Chl-a exchange near the mixed-layer base. Here we further examine the dynamical pathway linking mesoscale eddy modulation of the mixed layer to low-Richardson-number frontal regimes. The analysis focuses on the representative section ft34-820-22, which provides the clearest continuous transect across multiple eddy-edge environments.

The mixed layer depth (MLD) along the representative section shows a pronounced large-scale seasonal evolution, with progressive deepening during the austral winter and spring (Fig. S1a). To separate this seasonal background from mesoscale variability, we applied a 31-point along-track moving mean to the raw MLD and defined the residual as the MLD anomaly, MLD'. The same filtering procedure was applied to sea level anomaly (SLA) to obtain SLA' (Fig. S1b). This decomposition isolates the local mesoscale modulation superimposed on the basin-scale and seasonal MLD evolution.

After removal of the background field, SLA' and MLD' show a statistically significant positive relationship (Fig. S1c; $N = 433,\ r = 0.177,\ p < 0.01$). The regression slope is 72.7 m m^{-1}, indicating that a 0.1 m positive SLA anomaly is associated with an average MLD deepening of 7.27 m. This relationship is consistent with a reduced-gravity interpretation, in which positive sea-level anomalies associated with anticyclonic mesoscale features correspond to a deeper upper-ocean interface. Although the seasonal MLD trend provides the large-scale background, the residual SLA–MLD relationship indicates that mesoscale eddies impose a significant local modulation on the depth of the mixed-layer base.

This mesoscale modulation provides a preconditioning mechanism for eddy-edge exchange. Spatial variations in SLA and MLD create a sloping mixed-layer base near eddy boundaries. This sloping interface sharpens lateral buoyancy gradients and enhances isopycnal slopes close to the transition between the mixed layer and the stratified interior. Such frontal geometry favors submesoscale secondary circulation and low-Richardson-number regimes near the mixed-layer base, providing a physical setting for localized vertical exchange.

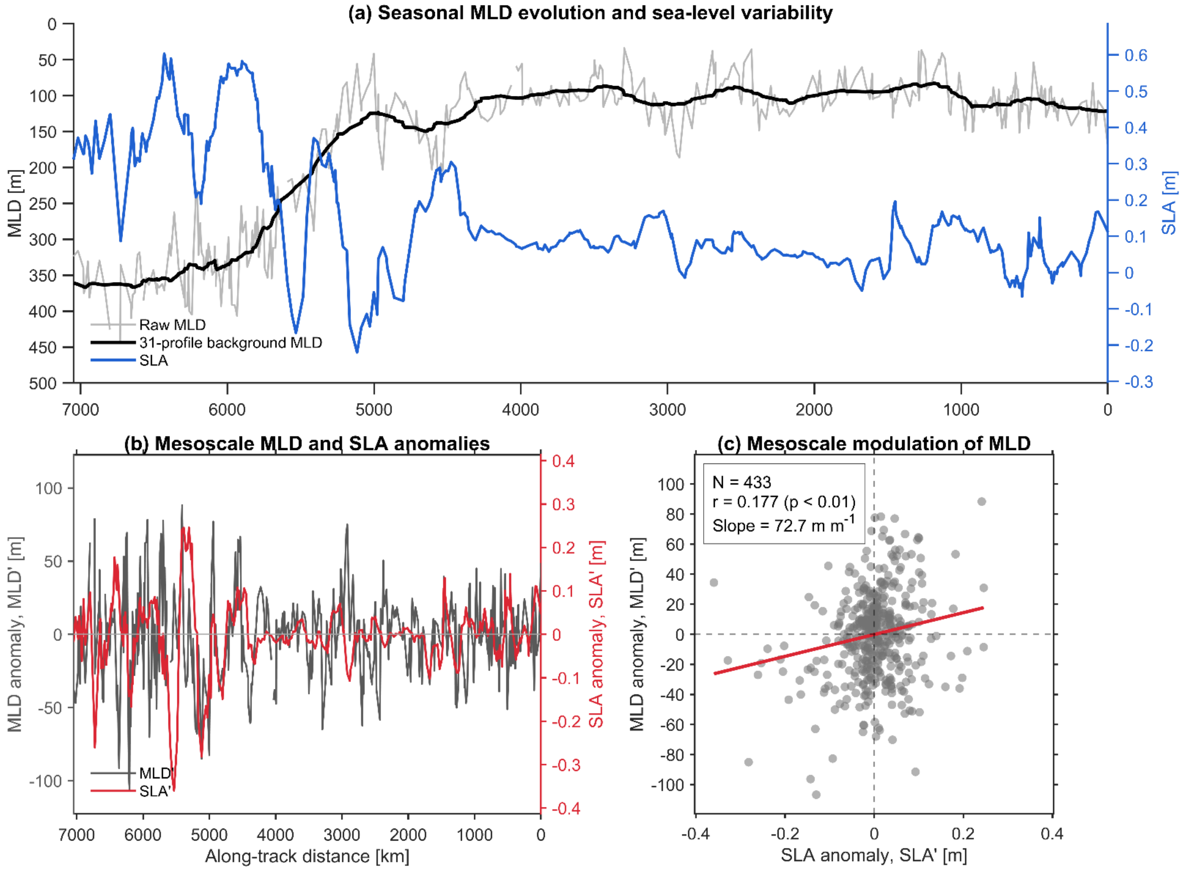

Figure S1. Mesoscale modulation of mixed layer depth along the representative seal section.
(a) Along-track mixed layer depth (MLD), 31-point moving-mean background MLD, and sea level anomaly (SLA) along the representative section ft34-820-22. The raw MLD shows a large-scale seasonal deepening, whereas SLA provides the mesoscale sea-level context. (b) Along-track anomalies of MLD and SLA after removal of the 31-point moving-mean background. (c) Scatter plot between SLA' and MLD'. The red line denotes the linear regression, with $N = 433$, $r = 0.177$, $p < 0.01$, and a slope of 72.7 m m^{-1}.

To diagnose the instability regime associated with the strongest vertical motions, we performed a conditional sampling analysis in the representative section ft34-820-22. The analysis was restricted to the layer between the MLD and 80 m below the MLD, corresponding to the interface zone where the main text identifies strong Chl-a exchange. Active grid cells were defined as the top 10% of $|w|$ among all valid grid cells in this layer. This subset contains 3350 valid grid cells, with a threshold value of $|w| = 0.24\ \mathrm{m\ d^{-1}}$ (Fig. S2b).

The instability regime of each active grid cell was classified using the geostrophic Richardson number,

$$Ri = \frac{f^2 N^2}{b_x^2},$$

where f is the Coriolis parameter, N^2 is the squared buoyancy frequency, and b_x is the cross-front buoyancy gradient. Three regimes were distinguished: shear-susceptible conditions $(Ri < 0.25)$, symmetric-instability-favorable conditions $(0.25 \leq Ri < 1)$, and higher-Ri conditions $(Ri \geq 1)$.

The regime distribution along the representative section shows that low-Ri conditions are widespread within the MLD to MLD+80 m layer, particularly along the sloping mixed-layer base and eddy-edge frontal transition zones (Fig. S2a). In the top 10% $|w|$ active cells, 57.58% of grid cells fall within $0.25 \leq Ri < 1$, indicating that SI-favorable conditions dominate the strongest vertical-exchange regions. A further 10.36% of active cells satisfy $Ri < 0.25$, indicating locally strong shear-susceptible conditions. The remaining 32.06% are characterized by $Ri \geq 1$.

Together, the SLA–MLD relationship and Richardson-number classification establish a consistent dynamical pathway. Mesoscale eddies locally modulate the mixed-layer base, producing sloping MLD structures near eddy edges. These sloping interfaces intensify frontal buoyancy gradients and favor low-Ri regimes near the mixed-layer base. The strongest diagnosed vertical motions preferentially occur within these SI-favorable and shear-susceptible frontal environments, supporting the interpretation that eddy-edge preconditioning enables localized bidirectional Chl-a exchange across the mixed-layer base.

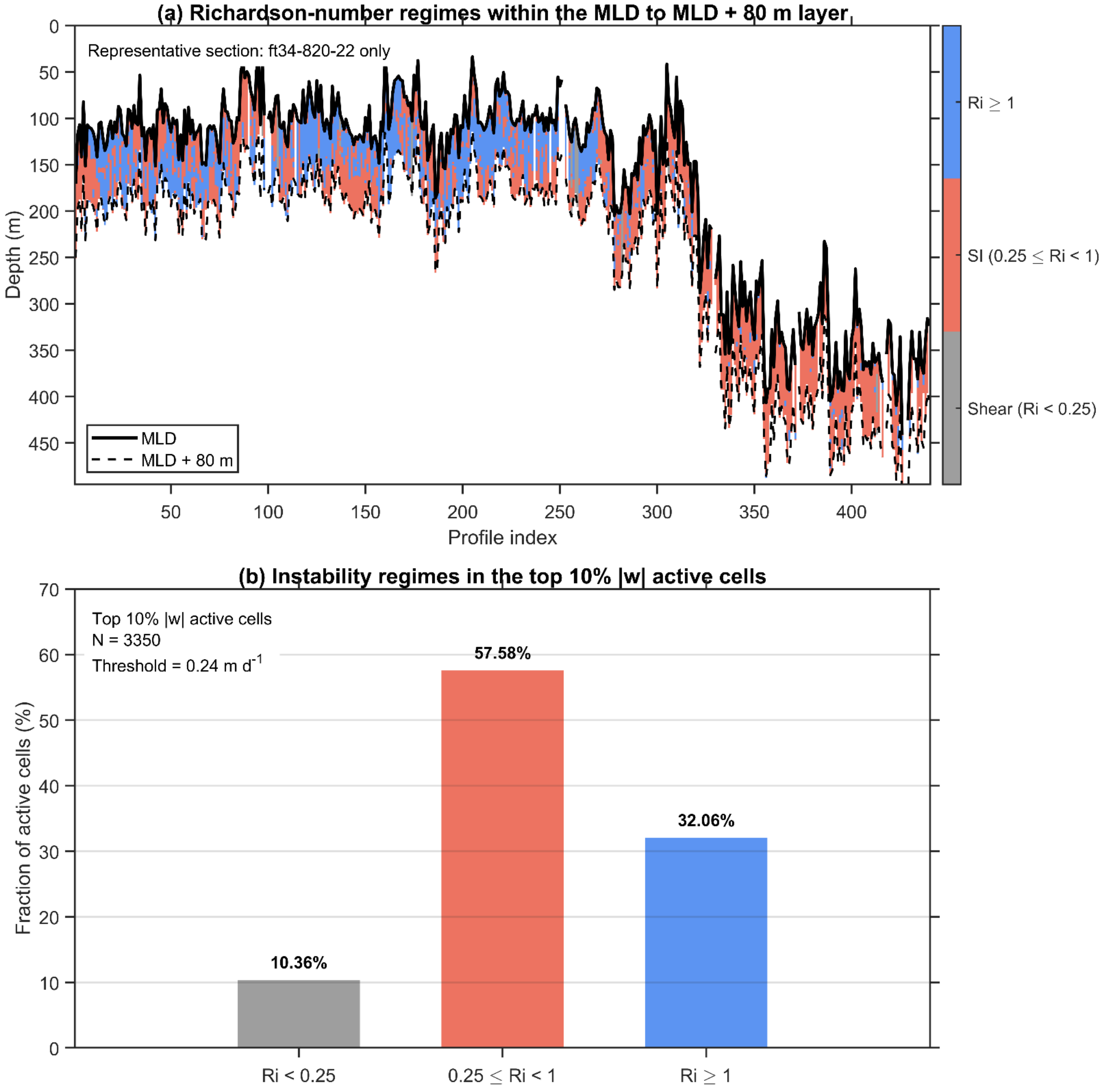

Figure S2. Richardson-number regimes in the MLD to MLD+80 m layer along the representative section ft34-820-22. (a) Spatial distribution of Richardson-number regimes between the MLD and 80 m below the MLD. The solid black curve denotes the MLD, and the dashed black curve denotes MLD+80 m. Colors indicate shear-susceptible conditions $(Ri < 0.25)$, symmetric-instability-favorable conditions $(0.25 \leq Ri < 1)$, and higher-Ri conditions $(Ri \geq 1)$. (b) Fraction of instability regimes within the top 10% $|w|$ active cells. Active cells were selected from all valid grid cells between the MLD and MLD+80 m along ft34-820-22. The active subset contains 3350 grid cells, with a $|w|$ threshold of 0.24 m d^{-1}.

Richardson-number-based regime classification and sensitivity test

The QG omega-equation diagnosis provides the balanced component of the vertical velocity associated with the observed frontal density field and satellite-constrained strain forcing. In eddy-edge frontal environments, this balanced secondary circulation can coexist with ageostrophic motions associated with symmetric instability, shear-susceptible instability and mixed-layer frontal adjustment. To characterize the dynamical regimes sampled by the seal trajectories, we used the geostrophic Richardson number,

$$Ri_g = \frac{f^2 N^2}{b_x^2},$$

where f is the local Coriolis parameter, $N^2 = \partial b / \partial z$ is the squared buoyancy frequency, and $b_x = \partial b / \partial x$ is the cross-front buoyancy gradient. Through thermal-wind balance, Ri_g is equivalent to a Richardson number based on the geostrophic vertical shear. Low Ri_g values therefore identify regions with steep isopycnals, strong geostrophic shear and frontal conditions favorable for ageostrophic vertical exchange.

We divided the frontal regimes into three diagnostic classes. Grid cells with $Ri_g < 0.25$ were classified as strongly shear-susceptible regions, cells with $0.25 \leq Ri_g < 1$ as symmetric-instability-favorable regions, and cells with $Ri_g \geq 1$ as relatively balanced or weakly unstable regions. This classification was used to evaluate where the strongest diagnosed vertical velocities and Chl-a transport occurred relative to the mixed-layer base and eddy-edge frontal structures.

To assess the sensitivity of the diagnosed Chl-a transport to possible ageostrophic enhancement under low-Ri_g conditions, we performed an additional amplitude-scaling experiment. In this test, the QG-derived vertical velocity was multiplied by a regime-dependent factor: 1.4 for $Ri_g < 2$, 1.2 for $2 \leq Ri_g \leq 10$, and 1.1 for $Ri_g > 10$. The largest enhancement was therefore applied to the lowest-Ri_g frontal regions, where ageostrophic exchange is expected to be most active, while weaker enhancement was applied to more balanced regimes. This scaled velocity field was used only for sensitivity testing; the primary analyses and figures are based on the unscaled QG-derived vertical velocity.

The Ri-dependent scaling increased the amplitude of the diagnosed Chl-a transport but preserved its spatial organization and sign structure. Strong upward and downward Chl-a transport remained concentrated near eddy edges and close to the mixed-layer base, and the same localized exchange patterns appeared in both the unscaled and scaled calculations. This sensitivity test shows that the main results are robust to reasonable amplitude enhancement in low-Ri_g regimes. The spatial concentration of strong Chl-a transport is controlled primarily by the observed frontal buoyancy gradients, satellite-constrained strain field and Chl-a structure, rather than by the specific amplitude-scaling choice.

Eddy-centric collocation and coordinate normalization

To examine how vertical exchange varies with position relative to mesoscale eddies, we constructed an eddy-centric coordinate system using the AVISO+ Mesoscale Eddy Trajectories Atlas (META3.2exp NRT). For each seal profile, cyclonic and anticyclonic eddy candidates within a temporal window of ± 0.5 days were identified. The geographic distance d between the profile location and each eddy center was calculated using the Haversine formula and normalized by the effective eddy radius R provided by the eddy atlas. When multiple eddies were located near the same profile, the eddy with the smallest normalized distance d/R was assigned to that profile.

The normalized radial coordinate was defined as

$$r/R = d/R,$$

where $r/R = 0$ represents the eddy center and $r/R \approx 1$ represents the effective eddy boundary. This normalization allows observations from eddies of different sizes to be compared within a common radial framework. Cyclonic and anticyclonic eddies were composited separately to evaluate polarity-dependent differences in vertical velocity, hydrographic structure and Chl-a transport.

For regional comparisons, profiles were divided into three eddy-centric zones: the eddy core $(0 \leq r/R < 0.8)$, the eddy edge $(0.8 \leq r/R \leq 1.2)$, and the surrounding background $(1.2 < r/R \leq 2.5)$. The eddy-edge band was centered on the effective eddy boundary and was used to represent the region of strongest mesoscale shear and frontal deformation. Profiles outside $r/R = 2.5$ were excluded from the eddy-centric composites.

Table S1:

Summary of seal-borne observational profiles. Valid QG profiles refer to data retained after trajectory gap screening, hydrographic quality control and quasi-geostrophic (QG) diagnostic criteria. Track length and profile spacing are calculated from consecutive profile locations along each trajectory. Values in square brackets represent the interquartile range (IQR). A 1 m vertical grid is adopted for data interpolation, while horizontal sampling resolution is represented by along-track profile spacing.

Platform ID	Period	Profiles	Valid QG	Valid Chl-a	Track length (km)	Profile spacing (km, median [IQR])	Latitude range	Longitude range	MLD (m, median [IQR])
ft33-469-22	2023-05-30 to 2023-10-05	435	435	315	6987.1	11.92 [5.15-22.26]	-66.94 to -53.40	-180.00 to 179.99	121.8 [100.3-152.6]
ft33-752-22	2023-06-08 to 2023-11-11	485	473	362	8314.2	13.50 [6.30-24.63]	-58.79 to -49.11	148.36 to 165.71	204.1 [133.8-311.0]
ft33-787-22	2023-05-30 to 2023-12-05	659	659	540	9893.9	11.47 [4.89-22.14]	-65.93 to -54.16	157.50 to 171.39	111.9 [90.1-135.4]
ft34-813-22	2023-06-01 to 2023-07-02	95	85	73	1847.6	15.70 [6.28-28.74]	-59.00 to -54.45	155.31 to 159.02	100.5 [75.3-128.8]
ft34-814-22	2023-05-20 to 2023-11-20	570	568	457	10637.6	13.87 [6.52-25.80]	-64.71 to -46.72	137.48 to 160.67	131.7 [92.1-282.6]
ft34-820-22	2023-05-23 to 2023-10-17	440	431	346	7040	12.42 [5.66-24.64]	-63.51 to -54.41	155.17 to 166.53	114.9 [97.8-234.4]
All platforms	2023-05-20 to 2023-12-05	2684	2651	2093	44720.3	12.75 [5.61-23.73]	-66.94 to -46.72	-180.00 to 179.99	122.8 [96.1-204.0]

Table S2:

Definitions and units of diagnostic variables.

Quantity	Definition	Unit	Physical meaning
w	QG-derived vertical velocity	m d^{-1}	diagnosed balanced vertical velocity
w'	$w - \langle w \rangle_{31}$	m d^{-1}	submesoscale vertical velocity anomaly
F_C	$w'C$	mg m^{-2} d^{-1}	signed vertical Chl-a transport
E_C	$\lvert w' \rvert C$	mg m^{-2} d^{-1}	absolute exchange intensity
I_C	$\int_0^{250m} F_C \, dD$	mg m^{-1} d^{-1}	below-MLD integrated Chl-a transport
A_C	$w' \, \partial C / \partial D$	mg m^{-3} d^{-1}	local Chl-a advective tendency
A_{cold}	$-w' \, \partial T / \partial D$	°C d^{-1}	cold-water injection proxy
Ri_g	$f^2 N^2 / b_x^2$	dimensionless	geostrophic Richardson number
r/R	d/R	dimensionless	eddy-centric radial coordinate

Table S3:

Profiles were collocated with mesoscale eddies using the AVISO+ Mesoscale Eddy Trajectories Atlas and assigned to anticyclonic (AC) or cyclonic (CY) eddies according to the minimum normalized distance d/R, where d is the distance from the eddy center and R is the effective eddy radius. The eddy-centric radial zones were defined as core ($0 \leqslant r/R < 0.8$), edge ($0.8 \leqslant r/R \leqslant 1.2$), and background ($1.2 < r/R \leqslant 2.5$). “Profiles” denotes the number of seal profiles assigned to each polarity–zone class. “Valid Chl-a profiles” denotes profiles with available Chl-a observations used for the vertical Chl-a transport analysis near the mixed-layer base. The fraction within polarity was calculated separately for AC and CY eddies.

Eddy	zone	Profiles	Valid Chl-a profiles	Fraction within polarity (%)
AC	Core	330	78	35.3
AC	Edge	251	120	26.8
AC	Background	355	241	37.9
AC total	Total	936	439	100
CY	Core	196	127	29
CY	Edge	232	138	34.3
CY	Background	248	163	36.7
CY total	Total	676	428	100

Table S4:

Intermittency of layer-integrated Chl-a transport. The table summarizes the fraction of total upward and downward layer-integrated Chl-a transport I_C captured by the strongest 10–40% of the along-track footprint. I_C was calculated by vertically integrating the signed vertical Chl-a transport F_C over the upper 250 m. Downward $(I_C < 0)$ and upward $(I_C > 0)$ contributions were treated separately by sorting profiles according to the magnitude of their directional contribution. Values correspond to the cumulative contribution curves shown in Figure 5c.

Transport direction	Directional profiles	Top 10% directional footprint (%)	Top 20% directional footprint (%)	Top 30% directional footprint (%)	Top 40% directional footprint (%)	Total directional I_C
Downward I_C < 0	1063	74.8	88.1	93.9	96.8	-2.08E+04
Upward I_C > 0	997	70.7	85.4	92.3	96	1.45E+04